α-Fe₂O₃/NiOOH: An Effective Heterostructure for Photoelectrochemical Water Oxidation

Francesco Malara,[†] Alessandro Minguzzi,[‡] Marcello Marelli,[†] Sara Morandi,[‡] Rinaldo Psaro,[†] Vladimiro Dal Santo,*,[†] and Alberto Naldoni*,[†]

[†]CNR-Istituto di Scienze e Tecnologie Molecolari, Via Golgi 19, 20133 Milan, Italy
[‡]Dipartimento di Chimica, Universitá degli Studi di Milano, Via Golgi 19, 20133 Milan, Italy

Ⓢ Supporting Information

ABSTRACT: The study of the semiconductor/electrocatalyst interface in electrodes for photoelectrochemical water splitting is of paramount importance to obtain enhanced solar-to-fuel efficiency. Here, we take into consideration the multiple effects that a thin layer of photodeposited amorphous Ni-oxyhydroxide (NiOOH) induces on hematite (α-Fe₂O₃) photoanodes. The reduction of overpotential produced a photocurrent onset potential advance of 150 mV and an increase of photocurrent of about 50% at 1.23 V vs RHE. To give an interpretation to these phenomena, we carried out deep electrochemical investigations by cyclic voltammetry and electrochemical impedance spectroscopy. The effective charge injection into the electrolyte due to the reduction of the charge transfer resistance at the electrode/electrolyte interface was observed and increased along with the amount of deposited NiOOH. The benefits of NiOOH deposition are ascribable to its ability to scavenge holes from hematite surface traps. This effect is mitigated at a potential higher than 1.25 V, since a fraction of photogenerated holes is consumed into the Ni redox cycle.

KEYWORDS: water splitting, hematite, semiconductor, electrocatalyst, electrochemical impedance spectroscopy, nickel oxyhydroxide
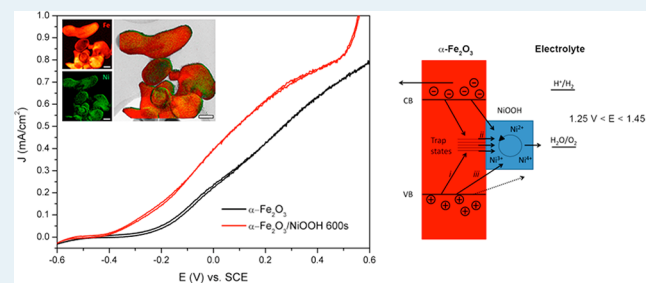
■ INTRODUCTION

The production of solar fuels in a photoelectrochemical (PEC) water splitter is a promising technology toward the use of renewable energy and chemical feedstocks.[1,2] The most effective approach to water splitting is to build multilayer photoelectrodes where the semiconductor works as an antenna for light absorption, while the electrocatalyst reduces the overpotential (η) for the hydrogen or the oxygen evolution reaction (HER and OER, respectively).[1,2] In a PEC cell, the development of efficient photoanodes is extremely challenging, as one has to achieve the difficult match among high charge mobility, an optimal band gap, and stability under anodic conditions.[3]

Hematite (α-Fe₂O₃) is a very attractive semiconductor for water oxidation due to its high absorption of visible light, excellent stability in alkaline media, low cost, and high abundance of iron.[4,5] However, to reach the minimum solar-to-hydrogen efficiency required to produce real devices, i.e. 10%, several processes must be optimized.

The deposition of an electrocatalyst (e.g., IrOₓ, Co-Pi, CoOₓ) or a passivation layer (e.g., Al₂O₃, Ga₂O₃) often improves the photocurrent onset potential of α-Fe₂O₃.[6−10] Some authors have observed that the use of the former leads to an improvement in the hole transfer at the electrode/electrolyte interface,[11,12] while the latter produces an enhanced photo-

voltage, probably because of the passivation of surface trap states.[8]

The different researchers' conclusions strongly suggest that the basic understanding of the process occurring at the semiconductor/overlayer interface should be improved. This aspect is crucial in order to obtain efficient charge separation and hence a high solar-to-fuels conversion.[13]

We present a detailed study on the PEC activity of α-Fe₂O₃ photoanodes covered with an Ni-oxyhydroxide layer that aims to evaluate the charge separation capabilities of the new interface, the effect of Ni redox activity on hole transfer, and the OER overpotential decrease.

Hydrous Ni-based electrocatalysts have shown very high activity toward OER.[14−20] In particular, Boettcher et al. have shown that the deposition of NiOOH onto a TiO₂ electrode produces not only an improvement of the rate of electron transfer to the solution but also a new equilibrium and nonequilibrium interface energetics.[21,22] Comparing the electrical behavior of high conductivity/crystalline (i.e., IrOₓ) and ion-permeable/hydrous (i.e., NiOOH) catalysts on TiO₂, they found that the first type induced the formation of a buried junction, while the second type formed an adaptive junction
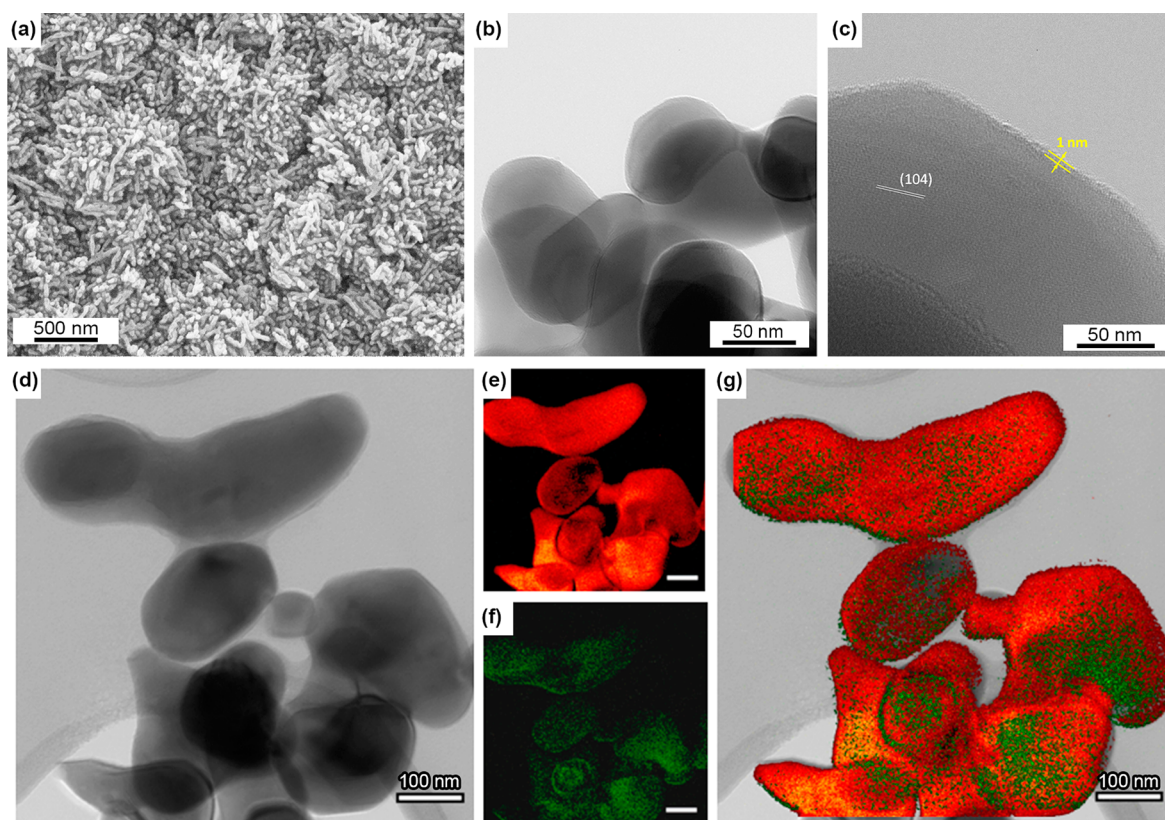
Figure 1. (a) SEM image of the α-Fe$_2$O$_3$ electrode. (b) TEM image of the coral-like α-Fe$_2$O$_3$ nanostructures. (c) Magnification of a α-Fe$_2$O$_3$ single particle after NiOOH photodeposition showing its amorphous nature. (d) TEM micrograph and related elemental distribution ESI map of (e) Fe (red) and (f) Ni (green) on α-Fe$_2$O$_3$ covered by a thin layer of NiOOH. (g) Representation obtained from the overlapping of TEM and element-filtered images.

where the effective interface barrier height, and hence the photovoltage output of the electrode, changes depending on the oxidation state of the electrocatalyst.

Here, we show the effects of a thin amorphous NiOOH layer on the PEC properties of α-Fe$_2$O$_3$ photoanodes. A significant improvement of activity toward OER under AM 1.5 illumination was obtained in terms of enhancement of maximum photocurrent and cathodic shift of onset potential (about 150 mV). Impedance spectroscopy and Mott−Schottky measurements revealed that NiOOH catalyst deposition reduces charge recombination at the electrode/electrolyte interface and promotes the collection of superficial charges. In addition, above a certain potential value, the NiOOH oxidation processes limit the generated photocurrent due to recombination phenomena at the α-Fe$_2$O$_3$/NiOOH interface.

■ EXPERIMENTAL SECTION

Thin films of α-Fe$_2$O$_3$ were deposited on fluorine-doped tin oxide (FTO)-coated glass substrates (Solaronix, 10 Ω/sq). Deposition took place at 70 °C for 3 h using a precursor aqueous solution of FeCl$_3$·6H$_2$O (0.15 M) and NaNO$_3$ (1 M), at pH 1.5 optimized with HCl.[23] After the synthesis, samples were gently rinsed with deionized water and then calcined at 500 °C for 1 h, followed by 20 min at 800 °C.[24]

α-Fe$_2$O$_3$/NiOOH junctions were synthesized through a modified photo-/electrodeposition procedure.[25] α-Fe$_2$O$_3$ electrodes were immersed in a 0.1 M Ni(NO$_3$)$_2$ solution with pH adjusted to 6.6 by adding NaOH. Prior to the photodeposition of NiOOH, the solution was purged with nitrogen gas for 1 h.

Photodeposition was carried out in a three-electrode PEC cell at open circuit voltage (V_{oc}), by using a Ag/AgCl reference electrode (RE) and Pt mesh as counter electrode (CE). Different photodeposition times were tested: 60, 300, 600, and 1200 s. The photodeposition was followed by an electrodeposition at 1.2 V vs Ag/AgCl for 60 s.

X-ray diffraction (XRD) measurement was performed at room temperature in the $20° \leq 2\theta \leq 70°$ range employing Cu Kα radiation at room temperature. Diffraction data were collected by directly placing the FTO films within the sample holder of the diffractometer.

Scanning electron microscopy (SEM) analysis of scaffolds were acquired by using a LEO 1430 at 20 kV and a working distance of 10 mm. TEM analyses were carried out with a ZEISS LIBRA200FE. Electron spectroscopic imaging (ESI) data were collected to map the elemental distribution of Fe and Ni via energy-filtering electrons at the corresponding electron energy loss (EEL). Iron and nickel were prepared at their L$_3$ edges. A three-window methodology was used with a LIBRA200 in column ω-filter spectrometer. TEM specimens were prepared by scratching the electrode surface and collecting the particles by adherence onto a holey carbon coated copper grid.

The electrodes were electrochemically characterized in a three-electrode system: the RE was a saturated calomel electrode (SCE), while a high-surface-area Pt mesh was the CE. E was referred to the reversible hydrogen electrode (RHE) scaled through the Nernst equation:

$$E_{RHE} = E_{SCE} + 0.244\ V + 0.059 pH$$

where E_{SCE} is the measured electrode potential vs the reference electrode used and 0.244 is the reference electrode standard potential vs the normal hydrogen electrode. Below, all measurements will be reported with respect to the RHE. The measurements were carried out in 1 M NaOH aqueous solution at pH 13.6. Cyclic voltammetry (CV) curves were measured at a scan rate of 10 mV/s. PEC measurements were made with a PGSTAT204 Autolab potentiostat. Electrochemical impedance spectroscopy (EIS) and data were gathered using a 10 mV amplitude perturbation at frequencies between 0.01 Hz and 1 MHz. Mott−Schottky analysis was performed in the dark at various frequencies between 1 and 1000 Hz. In particular, the values reported in Figure 8 were obtained at 1 kHz. A 300 W xenon arc lamp (calibrated at 100 mW/cm^2) coupled to an AM 1.5 G filter was used as the light source. The incident photon to current efficiency (IPCE) measurements were carried out by applying a set of band-pass filters (fwhm 40 nm, wavelength range 400−850 nm, Thorlabs) at the light source. At least three electrodes of each type were fabricated and tested. All electrodes showed similar characteristics, and representative data are reported.

Scanning electrochemical microscopy (SECM) experiments were carried out in a four-electrode cell configuration where the substrate was the WE1, while the SECM tip was the WE2. The latter consisted of a 25 μm diameter gold wire (Goodfellow, 99.99% purity), sealed into a flint glass capillary with o.d./i.d. 1.5/0.75 mm (#27-37-1, Frederik Haer & Co., Bowdoinham, ME) under vacuum. A graphite rod as the CE and Ag|AgCl 3 M KCl as the RE completed the equipment. To minimize the contamination with chlorine ions, the reference electrode was separated from the solution by a salt bridge consisting of a glass pipet filled with agar, containing 0.1 M aqueous KClO$_4$. All experiments were carried out in 1 M NaOH and after the tip was approached at about 5 μm far from the sample. The SECM tip was biased at a constant potential of 1.2 V, while a stair-step potential profile (ΔE = 5 mV; Δt = 30 s) between 0.5 and 1.6 V was applied to the substrate. The tip current was selected in order to reduce O$_2$ to water under mass transport control.[26] During each measurement, the sample was kept under illumination by means of a solar simulator.

■ RESULTS AND DISCUSSION

Figure 1a shows a representative SEM image of the surface morphology of α-Fe$_2$O$_3$ obtained through thermal solution synthesis. The FTO substrate was uniformly covered with dense nanocorals.[23] A TEM analysis highlighted the fact that the nanocorals are formed by interconnected crystalline globular grains (Figure 1b). The main reflections on the XRD pattern (Figure S1 in the Supporting Information) were assigned to the SnO$_2$ (cassiterite phase, space group $P4_2/mnm$) related to the FTO, whereas the weak diffraction peaks indexed as (110) and (300) belong to α-Fe$_2$O$_3$ ($R\bar{3}c$ H setting). By taking the diffraction pattern for powdered α-Fe$_2$O$_3$ sample as a reference, the complete extinction of (hkl) peaks with $l \neq 0$ indicated a strong orientation of (001) crystallographic planes perpendicular to the conductive glass surface.[10]

After the photo-/electrodeposition cycle, a thin NiOOH amorphous layer of 1−2 nm ca. covered the α-Fe$_2$O$_3$ nanostructures (Figure 1c,d). From the ESI filtered maps (Figure 1e,f) it is clear that the bulk of each grain was enriched with Fe, while the outer layer was a Ni-rich phase (Figure 1g).

Figure 2 shows the CV in the dark for bare α-Fe$_2$O$_3$ and NiOOH-modified samples at different photodeposition times,
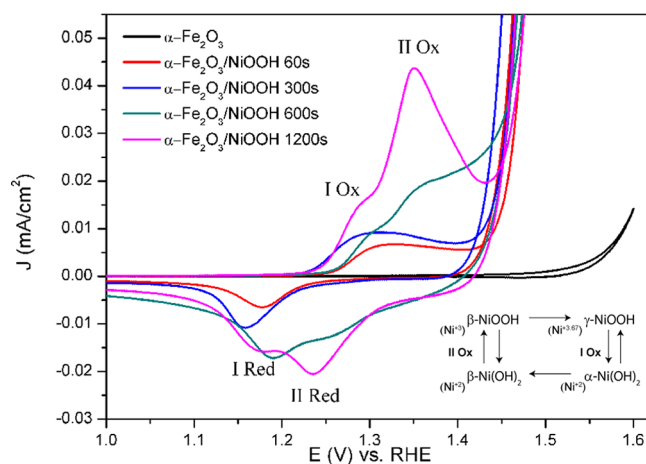

Figure 2. Cyclic voltammetry of bare α-Fe$_2$O$_3$ (dark line) and α-Fe$_2$O$_3$/NiOOH electrodes obtained at different NiOOH photo-deposition time (colored lines) in NaOH solution (1 M) in the dark. The inset reports the Bode cycle for the Ni(II)/Ni(III) redox transitions in Ni hydroxide layers.

carried out to evaluate the electrocatalytic activity of the electrodes. For the former, the dramatic increase of photo-currents at 1.55 V suggested the OER onset. The same phenomena for all α-Fe$_2$O$_3$/NiOOH electrodes began at 1.40 V. The overpotential (η) toward the OER for the NiOOH-modified photoanodes was in the range 232−242 mV. These values are much lower in comparison to those of α-Fe$_2$O$_3$/IrO$_x$ (i.e., η = 300 mV) electrodes[10] and are in agreement with values obtained for other electrocatalysts deposited through a similar procedure.[27] Interestingly, Selloni and co-workers[28] reported a computed η = 260 mV for the Fe-doped β-NiOOH phase. This result suggests an intimate contact between α-Fe$_2$O$_3$ and NiOOH. The higher slopes in the CV of α-Fe$_2$O$_3$/NiOOH and the η decrease indicated that a highly active NiOOH layer was deposited onto the α-Fe$_2$O$_3$ surface.[20]

In particular, the change in the CV of Ni-containing electrodes was attributed to the in situ formation of Ni(OH)$_2$/NiOOH hydroxide/oxyhydroxide species during the electrochemical conditioning process.[20] The layered Ni(OH)$_2$/NiOOH structure is composed of weakly interacting hydroxide layers that allow the intercalation of water and anions and therefore bulk redox activity.[29]

Following the Bode cycle (see inset Figure 2), the first oxidation wave (I Ox) around 1.29 V was assigned to the reversible α-Ni(OH)$_2$/γ-NiOOH transformation,[30,31] while the second pair of peaks (II Ox) were due to the β-Ni(OH)$_2$/β-NiOOH transformation. Corrigan et al. have assigned the former to a Ni^{2+}/Ni$^{3.67+}$ redox process, implying an ultimate limit of 1.67 e per Ni as opposed to the simple 1-electron Ni^{2+}/Ni^{3+} process.[32] Following this peak assignment, we can suggest that, after 60 and 300 s of photodeposition and electrochemical conditioning, α-Fe$_2$O$_3$/NiOOH photoanodes were mainly constituted of γ-NiOOH, whereas 600 and 1200 s samples contained both β-NiOOH and γ-NiOOH.

Figure 3a shows the photocurrent measured under AM 1.5 illumination for bare α-Fe$_2$O$_3$ and α-Fe$_2$O$_3$ electrodes prepared with different NiOOH photodeposition times (60, 300, 600, and 1200 s). All the photoanodes modified with NiOOH showed a photocurrent increase at 1.23 V and a cathodic shift of the onset potential in comparison to the α-Fe$_2$O$_3$ reference. The best-performing samples were those obtained at high
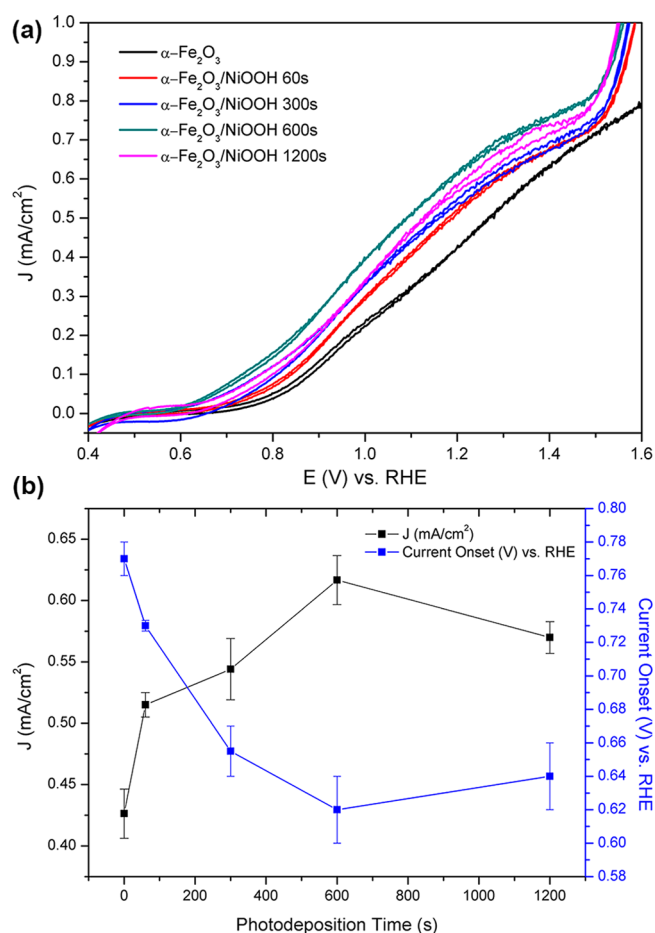
Figure 3. (a) Cyclic voltammetry under AM 1.5 illumination of untreated α-Fe$_2$O$_3$ and α-Fe$_2$O$_3$/NiOOH electrodes obtained at different photodeposition times. (b) Trends of current density and current onset vs photodeposition time (s).

photodeposition time (e.g., 600 and 1200 s). In particular, the α-Fe$_2$O$_3$/NiOOH sample at 600 s was the most active, showing a 47% increase of photocurrent density, from 0.425 mA/cm^2 (bare α-Fe$_2$O$_3$) to 0.625 mA/cm^2 at 1.23 V, and a cathodic shift of current onset potential of about 150 mV, from 0.78 to 0.62 V.

In Figure 3b, we report the trend of current density and current onset with respect to the photodeposition time. Both trends show that the values reached a plateau after 600 s of Ni photodeposition. The IPCE values of bare α-Fe$_2$O$_3$ and α-Fe$_2$O$_3$/NiOOH 600 s at 1.23 V are 9 and 19%, respectively, at 400 nm (Figure S2 in the Supporting Information).

Furthermore, it is worth mentioning that at 1.25 V < E < 1.45 V the photocurrent slope of the Ni-covered samples decreased, suggesting a decrease in the O$_2$ evolution rate.

Finally, at potentials higher than 1.5 V a strong increase of the current density with respect to the bare α-Fe$_2$O$_3$ electrode is evident and was attributed to the high electrochemical OER activity of the NiOOH amorphous layers.[29]

The long-term stability test shown in Figure S3 in the Supporting Information demonstrated that bare α-Fe$_2$O$_3$ and α-Fe$_2$O$_3$/NiOOH presented a stable steady-state production of O$_2$ also after 12 h of continuous PEC operation. We noted that the higher stability of the NiOOH-coated photoelectrode supports a stability effect in addition to the photoefficiency improvement demonstrated here.

In order to validate the beneficial effect of the NiOOH layer on the photoconversion efficiency and to prove that oxygen is the only reaction product, a set of substrate generation/tip-collection mode analysis has been carried out by scanning electrochemical microscopy (SECM).

In these experiments, a gold microelectrode is set at a desired distance from the sample surface (in this case 5 μm) by stopping an approach curve (1 μm s^{-1}) when the tip current reaches the value predicted by empirical negative feedback equations.[33] Using this setup, it is possible to use the tip as a sensor for the local O$_2$ concentration, which is in turn proportional to the rate of O$_2$ production at the substrate, thanks to the following equation, valid at steady state:

$$I_{ss} = 4nFcDa \qquad (1)$$

where n is the number of electrons, F is the Faraday constant, c is the concentration of the redox species (O$_2$), D is the diffusion coefficient, and a is the tip radius.

Moreover, by application of a stair-step potential profile at the substrate, a fine determination of the reaction onset is possible,[34] ruling out any interfering process, such as a parasitic reaction (e.g., the oxidation of the electrode itself).

On comparison of the tip current (I_{tip}) recorded for a pure α-Fe$_2$O$_3$ electrode and for a α-Fe$_2$O$_3$/NiOOH electrode (Figure S4 in the Supporting Information), it is clear that the presence of the Ni oxy/hydroxide layer led to a cathodic shift of the OER onset by about 150 mV, thereby confirming the results suggested from the J$-$E curve (Figure 3a).

To investigate the reasons behind the performance improvement after NiOOH photodeposition on the α-Fe$_2$O$_3$ electrodes, we carried out EIS measurements. From EIS it is possible to extract charge transfer resistances and capacitances at different interfaces of the multilayer electrode, providing an insight into the phenomena occurring in the presence of the NiOOH catalyst.

Figure 4a shows the Nyquist plot of α-Fe$_2$O$_3$ and of α-Fe$_2$O$_3$/NiOOH 600 s electrodes carried out with irradiation at 0.85 V. In this condition, each curve is composed of three arcs, characterized by frequency values extracted from Bode phase plots. Figure 4b reports the equivalent circuit (EC) used to fit the EIS data obtained from 0.7 V up to 1.25 V under irradiation.[11,12,35−39] The assignation was made as follows. R_s was the solution resistance in series of a parallel RC that models the FTO/α-Fe$_2$O$_3$ interface ($R_{FTO/bulk}$ and $C_{FTO/bulk}$) at high frequencies ($\sim$10500 Hz), a resistance related to the rate of the trapping holes (R_{bulk}) and a capacitance of the bulk hematite (C_{bulk}), the latter incorporated into the EC by a constant phase element (CPE$_{bulk}$), which considers the space charge region of α-Fe$_2$O$_3$ ($\sim$150 Hz), a charge transfer resistance ($R_{interface}$), and a capacitance ($C_{interface}$) of the surface states (calculated through a constant phase element, CPE$_{interface}$) relative to the electrode/electrolyte interface ($\sim$2.2 Hz). Figure 4a shows that the third arc ($\sim$2.2 Hz) relative to the α-Fe$_2$O$_3$/NiOOH electrode is much smaller in comparison to that of the α-Fe$_2$O$_3$ electrode. In other words, NiOOH greatly promoted the charge transfer across the electrode/electrolyte interface and thus dramatically suppressed the electron−hole recombination.

In contrast, at potentials higher than 1.25 V, only two semicircles were detectable (see Figures S5 and S6 in the Supporting Information). For bare α-Fe$_2$O$_3$, the characteristic frequencies of capacitances to charge transport processes were 10480 and 150 Hz, while for the α-Fe$_2$O$_3$/NiOOH electrodes these were 10480 Hz and 12−28 Hz. For bare α-Fe$_2$O$_3$, the

(a)

(b)
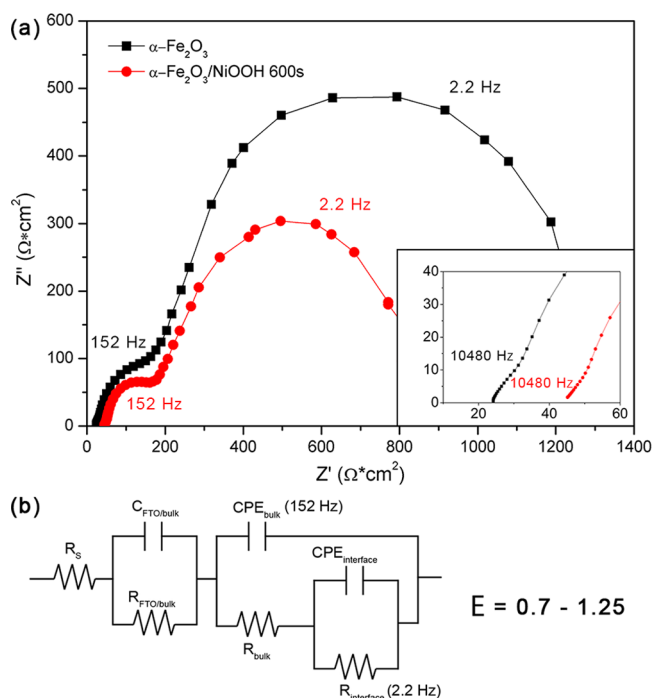
Figure 4. (a) Nyquist plot of bare α-Fe$_2$O$_3$ (dark squares) and α-Fe$_2$O$_3$/NiOOH 600 s (red circles) electrodes. The measurements were carried out at 0.85 V under illumination. The inset shows the enlargement of the high-frequency region to highlight the signal related to the FTO/α-Fe$_2$O$_3$. (b) Equivalent circuit used to fit and interpret EIS data at potentials 0.7 V < E < 1.25 V.

obtained parameters can be ascribed to the bulk (150 Hz), while those of the α-Fe$_2$O$_3$/NiOOH electrodes are ascribable to the α-Fe$_2$O$_3$/NiOOH interface (about 28 Hz).

To understand the frequency change under potential scan, we report also the Bode plot (Figure 5) of bare α-Fe$_2$O$_3$ and α-Fe$_2$O$_3$/NiOOH 600 s (i.e., the best-performing electrode) at three selected potentials: 0.7, 1, and 1.3 V.

A Bode plot represents the frequency response of a system to a sinusoidal perturbation: it is usually a combination of a magnitude plot, expressing the magnitude of the frequency response, and a phase plot, expressing the phase shift. Both quantities are plotted against a horizontal axis proportional to the logarithm of frequency. In Figure 5, we report the Bode phase plot, where each peak can be associated with a capacitance and a resistance in parallel, to which corresponds a characteristic frequency, given by $1/RC$. While the frequency values provide information relative to the time scale of the

processes, the phase values help in identifying the frequency domains relevant to a capacitive behavior. The higher the phase value, the more capacitive the behavior of the system, reflecting the accumulation of charge at a certain interface.

At 0.7 V both examined electrodes showed three main peaks centered around 2.2–5.17, 152–268, and 10480 Hz (the latter is not as well-defined in the Bode plot as much as in the Nyquist plot). At this potential the lowest frequency peak (2.2–5.17 Hz) of both electrodes showed higher phase value, suggesting that the charge transfer at the electrode/electrolyte interface was the limiting process in the PEC water oxidation.

At 1 V the peak's phase at 2.2–5.17 Hz was reduced and the peak at 152–268 Hz became predominant, suggesting that at this potential the reaction kinetics was limited by bulk (space charge region) phenomena.

At 1.3 V only one peak was visible for both α-Fe$_2$O$_3$ and α-Fe$_2$O$_3$/NiOOH 600 s. For the bare electrode the peak is centered at 152 Hz. In this case, at a potential higher than the thermodynamic potential of water splitting (i.e., 1.23 V), the oxygen evolution is limited only by the intrinsic properties of the semiconductor. Once we deposited NiOOH on α-Fe$_2$O$_3$, we observed the rise (Figure 5c) of a new peak at 12–28 Hz, lower than that of bare hematite (152 Hz), which implies a slower charge transfer kinetics. As reported above, at potentials 1.25 V < E < 1.45 V the slope of the J–E curve (Figure 3a) decreases and 1.3 V corresponds to the potential where Ni oxidation states are activated (see Figure 2). In the Ni-modified α-Fe$_2$O$_3$, holes that reach surface traps may be transferred to the surface-bound catalyst and injected into the electrolyte. At low potential this process is more effective, while for 1.25 V < E < 1.45 V some transient holes present in the NiOOH layer can be scavenged into the oxidation cycle of Ni(OH)$_2$/NiOOH, reducing the positive effect of the electrocatalyst.

Figure 6 shows the trend of capacitances at the electrode/electrolyte interface ($C_{interface}$ = 2.2 Hz) for all of the prepared photoanodes. At low potentials, $C_{interface}$ increased considerably at increasing NiOOH photodeposition time. This trend can be explained by the increased mass of deposited NiOOH that participates in capacitive phenomena and that exploits the high ionic permeability provided by the thin NiOOH layer.[29] In particular, α-Fe$_2$O$_3$/NiOOH 600 s, i.e. the best-performing samples, showed the highest $C_{interface}$ value.

All curves peaked in the potential window 0.8–1 V and were characterized by a flat region for E > 1 V. In particular, the α-Fe$_2$O$_3$ electrode showed the $C_{interface}$ maximum at 0.9 V, with NiOOH-modified electrodes instead peaking at 0.85 V (for 60, 300, and 1200 s of photodeposition) and 0.8 V for α-Fe$_2$O$_3$/
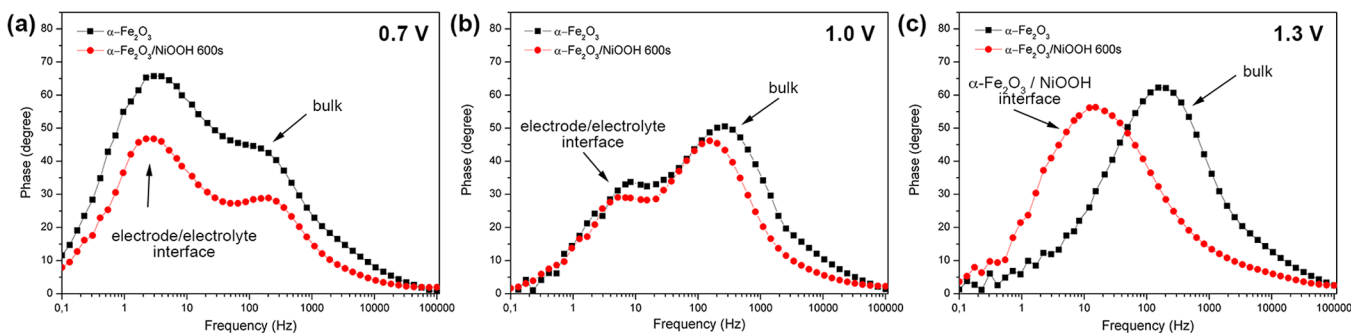
Figure 5. Bode plots for α-Fe$_2$O$_3$ (black circles) and α-Fe$_2$O$_3$/NiOOH 600 s (red circles) obtained at different potentials: (a) 0.7 V, (b) 1.0 V, and (c) 1.3 V.
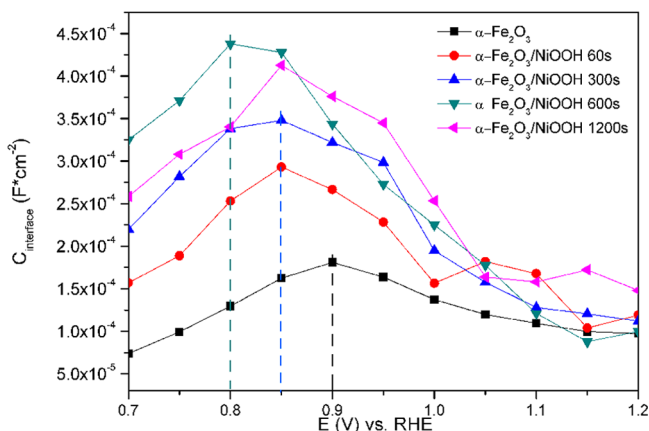
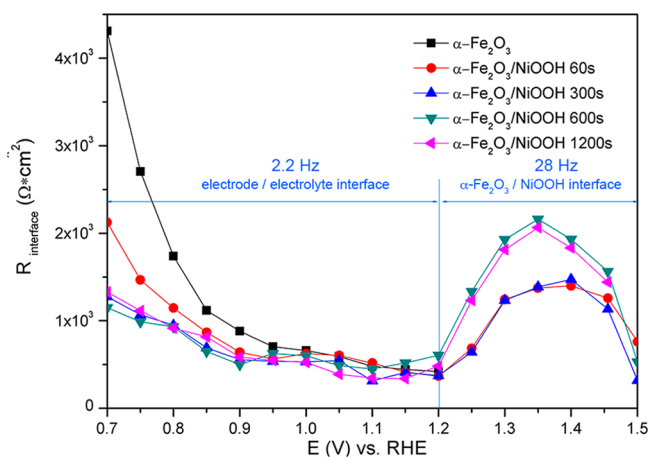**Figure 6.** Trend of capacitance at the electrode/electrolyte interface ($C_{interface}$ vs E) for α-Fe$_2$O$_3$ and α-Fe$_2$O$_3$/NiOOH electrodes obtained at different times of NiOOH photodeposition.

NiOOH 600 s: i.e., the electrode that shows the highest cathodic shift. The higher $C_{interface}$ values showed by the NiOOH-modified electrode are due to the high ionic permeability of Ni electrocatalyst. The $C_{interface}$ intensity and potential position correlated well with onset potential and plateau current of the investigated electrodes.

Figure S7 in the Supporting Information clearly shows that the C_{bulk} value was independent from NiOOH deposition: there was no difference between the C_{bulk} values of the bare electrode and the NiOOH-coated electrodes. In general, the C_{bulk} values decreased with an increase in the potential and the trend was essentially constant for all of the electrodes.

Figure 7 reports the trend of resistance both at the electrode/electrolyte interface ($R_{interface}$), corresponding to 2.2 Hz, and at the α-Fe$_2$O$_3$/NiOOH interface, corresponding to 28 Hz.

resistance can be due to a higher superficial contact area at the electrode/electrolyte interface after NiOOH deposition as well as due to a decrease of the number of surface traps. Moving toward anodic potentials, $R_{interface}$ values tend to conform, since charge transfer to the electrolyte is no longer the limiting process, as already evidenced by the $C_{interface}$ behavior (see Figure 6).

At $E > 1.2$ V, EIS measurements provided information on the α-Fe$_2$O$_3$/NiOOH interface, characterized by a frequency of 28 Hz. All of the plots peaked at about 1.35 V, corresponding to the oxidation wave involving the redox activity of Ni species. It is worth noting that $R_{interface}$ values for α-Fe$_2$O$_3$/NiOOH samples obtained at 600 and 1200 s, i.e. electrodes with higher amounts of Ni in high oxidation states, are 50% higher in comparison to the values for 60 and 300 s electrodes. This evidence confirmed that $R_{interface}$ at 28 Hz may be associated with hole transfer from α-Fe$_2$O$_3$ to NiOOH, leading to the formation of Ni in higher oxidation states.

In Figure S8 in the Supporting Information we plot R_{bulk} (152 Hz) vs potentials. R_{bulk} is on the order of hundreds of Ω cm^2 and increased monotonically toward anodic potential along with the increase of charge flow through the electrodes. The trends of R_{bulk} are similar for all samples. Between 0.7 and 1 V the values of R_{bulk} are 3 orders of magnitude lower than those of $R_{interface}$, confirming that in this potential range the charge transfer at the electrode/electrolyte interface is the limiting process. Above 1.2 V we can report only the values of the bare α-Fe$_2$O$_3$ electrode, because the recombination processes into α-Fe$_2$O$_3$/NiOOH move at 28 Hz, as discussed above.

To further investigate the semiconductor/electrocatalyst interface and elucidate the enhanced photocurrent due to NiOOH deposition, we carried out Mott−Schottky (M-S) measurements in the dark in the potential range from 0.6 to 1.4 V (Figure 8a).

Figure 7. Trend of charge transfer resistance at the electrode/electrolyte interface (2.2 Hz) from 0.7 to 1.2 V and charge transfer resistance at the α-Fe$_2$O$_3$/NiOOH interface (28 Hz) from 1.2 to 1.5 V of the α-Fe$_2$O$_3$/NiOOH electrodes.

Figure 8. Mott−Schottky plots for α-Fe$_2$O$_3$ and α-Fe$_2$O$_3$/NiOOH electrodes obtained at different times of NiOOH photodeposition.
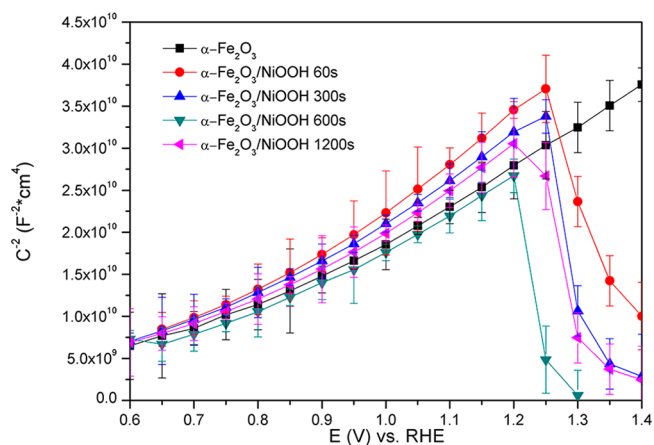
At low potentials (i.e., 0.7 V) α-Fe$_2$O$_3$ shows $R_{interface}$ = 4300 Ω cm^2. After 60 s of NiOOH photodeposition, $R_{interface}$ is reduced by approximately 50%, while for subsequent deposition times it was further reduced by 4 times in comparison to the bare α-Fe$_2$O$_3$. This difference between the $R_{interface}$ of the bare and NiOOH-coated samples can justify the cathodic shift of photocurrent onset.[23,24] The reduction of charge transfer

The bare electrode (black squares, Figure 8a) showed a positive slope, indicating that α-Fe$_2$O$_3$ is an n-type semiconductor with the electrons being the majority carriers. Differently, α-Fe$_2$O$_3$/NiOOH photoanodes exhibited the concomitant presence of positive and negative slopes, suggesting the formation of a p−n interface. The curves of the NiOOH-coated electrodes changed slope above 1.2−1.25 V, corresponding to the redox activity of Ni, when the Ni chemistry changes from a hydroxide to an oxyhydroxide phase,

leading to an altered electronic behavior. This change was anticipated when the NiOOH amount was increased and depended also on the composition of the NiOOH layer.[21,40]

From the M-S equation, the donor concentration (N_D) and the flat band potential (E_{FB}) can be extracted by

$$\left(\frac{A_s}{C_{bulk}}\right)^2 = \frac{2}{q\varepsilon_r\varepsilon_0 N_{D/A}}\left(V - E_{FB} - \frac{k_B T}{q}\right) \quad (2)$$

where C_{bulk} is the space charge capacitance, A_s is the area of the electrode, V is the applied potential, E_{FB} is the flat band potential of the semiconductor, k_B is the Boltzmann constant (1.38×10^{-23} J K^{-1}), T is the temperature (298 K), q is the electron charge (1.602×10^{-19} C), ε_0 is the permittivity under vacuum (8.85×10^{-12} C^2 J^{-1} m^{-1}), and ε_r is the dielectric constant (80 for α-Fe$_2$O$_3$).[41]

Table 1 reports the main parameters extrapolated by M-S measurements. Generally, the addition of an extremely thin

Table 1. Flat Band Potential (E_{FB}) and Donor Concentration (N_D) Values Extrapolated from Mott−Schottky Plots

	E_{FB} (V) vs RHE		N_D (cm^{-3})
	α-Fe$_2$O$_3$	NiOOH	
α-Fe$_2$O$_3$	0.513		1.24×10^{20}
α-Fe$_2$O$_3$/NiOOH 60 s	0.543	1.435	7.75×10^{19}
α-Fe$_2$O$_3$/NiOOH 300 s	0.524	1.348	1.07×10^{20}
α-Fe$_2$O$_3$/NiOOH 600 s	0.532	1.286	1.29×10^{20}
α-Fe$_2$O$_3$/NiOOH 1200 s	0.528	1.345	1.12×10^{20}

OEC layer should not affect the doping level or carrier density within the α-Fe$_2$O$_3$ electrode. Effectively, E_{FB} of α-Fe$_2$O$_3$ was not strongly affected by NiOOH deposition, being almost constant around 0.51−0.54 V for all samples. This small difference can be attributed to the change in the Helmholtz layer potential drop (V_H),[25] which is the only other factor that can affect the E_{FB} value, as shown in eq 3, where φ_{SC} is the work function of the semiconductor vs vacuum and 4.5 is the scale factor relating the H$^+$/H$_2$ redox level to vacuum.

$$E_{FB}(NHE) = \varphi_{SC} + V_H - 4.5 \quad (3)$$

The E_{FB} value of p-NiOOH depends slightly on the photodeposition time, moving from 1.435 V up to 1.286 V after 60 and 600 s of photodeposition, respectively. The N_D

values for all samples were quite similar (Table 1) for all samples.

Despite the M-S plot suggesting the formation of a p−n junction between NiOOH and α-Fe$_2$O$_3$, the free movement of ions into the electrocatalyst and the independence of C_{bulk} and R_{bulk} (Figures S7 and S8 in the Supporting Information) of the presence/absence of a NiOOH coating indicate that the formation of a p−n junction is not effective. This is in agreement with previous works on IrO$_x$ and CoPi catalysts on α-Fe$_2$O$_3$ electrodes.[12,42]

The photocurrent results from the generation of charge carriers by light absorption, separation of the charge carriers by the electrostatic field, and collection of the minority carriers (holes for an n-type semiconductor) by the contacting electrolyte. The photovoltage is limited by different primary recombination processes: bulk recombination, depletion region recombination, surface state recombination, and electron transfer.[43]

In Figure 9, we report the surface state recombination phenomena in a water-splitting process and the effect of Ni cocatalyst photodeposited on the α-Fe$_2$O$_3$ surface. In the bare α-Fe$_2$O$_3$ electrode (Figure 9a), holes are predominantly trapped in intragap states, where they slowly recombine with electrons (i). In the Ni-coated α-Fe$_2$O$_3$ (Figure 9b), holes can be partly scavenged by the surface-bound catalyst either via trap states (ii) or by direct transfer from the α-Fe$_2$O$_3$ valence band (iii) (VB). Recombination involves holes trapped both in the catalyst and in trap states.[44]

For bias values lower than 1.25 V (Figure 9b), the Ni compound is able to effectively scavenge the holes trapped into the α-Fe$_2$O$_3$ surface states, resulting in advanced photocurrent onset potential and faster photocurrent flow. Differently, for 1.25 V < E < 1.45 V (Figure 9c), the photocurrent density slope decreases because the holes scavenged by trapping sites are involved into the redox process of the Ni.

■ CONCLUSIONS

A series of photoanodes for water splitting composed by hematite and Ni-oxyhydroxide were prepared and studied to better understand the role of electrocatlyst on PEC activity and shed light on the semiconductor/electrocatalyst interface.

The optimized photo-/electrodeposition of NiOOH on α-Fe$_2$O$_3$ produced a 1−2 nm thick layer of amorphous electrocatalyst. The best performance was reached after 600 s of NiOOH photodeposition, resulting in a 50% increase of
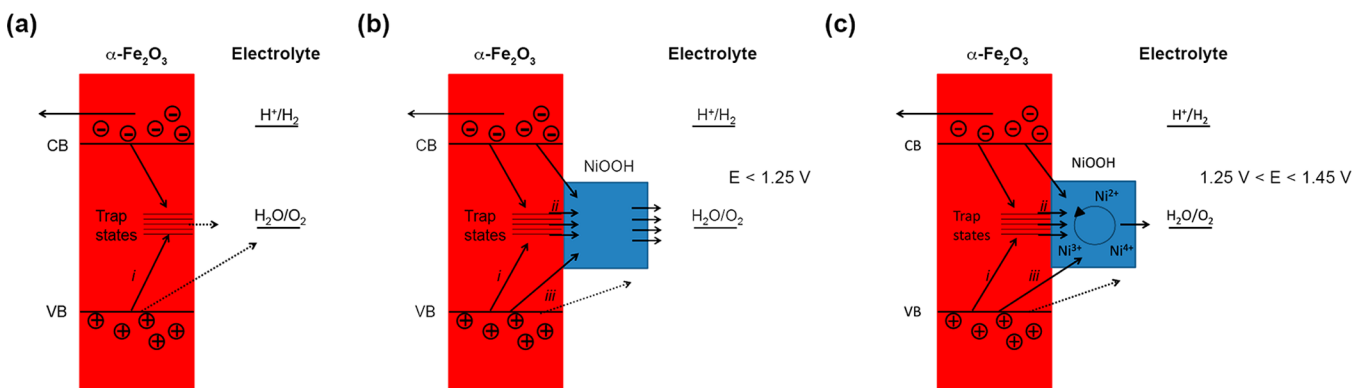
Figure 9. Scheme of surface state recombination phenomena in a water-splitting process for (a) bare α-Fe$_2$O$_3$, (b) α-Fe$_2$O$_3$/NiOOH at E < 1.25 V, and (c) α-Fe$_2$O$_3$/NiOOH at 1.25 V < E < 1.45 V.

photocurrent at 1.23 V and a 150 mV cathodic shift of the current onset potential.

Electrochemical impedance spectroscopy, on a wide potential range, revealed important features of the semiconductor/electrocatalyst system. At potentials between 0.7 and 1 V, the charge transfer resistance at the interface of the bare α-Fe$_2$O$_3$ was incredibly higher with respect to the NiOOH-coated electrodes. Since the NiOOH amorphous layer allowed an increased permeability of the ions reflected in the higher capacitance at the interface, it is possible to assign the reduction of resistance to a higher superficial contact area at the electrode/electrolyte interface as well as a passivation of the superficial trap sites. At higher potential ($E > 1.25$ V), instead, we observed a resistance associated with the new α-Fe$_2$O$_3$/NiOOH interface, having a characteristic frequencies of 28 Hz. This resistance appeared in correspondence of the Ni redox waves and was indirect evidence that the change in Ni oxidation states induced a new recombination process at the α-Fe$_2$O$_3$/NiOOH interface.

Understanding the semiconductor/electrocatalyst interface is important for optimizing the charge separation process in multilayer photoelectrodes and thus enhancing solar fuel yield in PEC devices.

■ ASSOCIATED CONTENT

Ⓢ Supporting Information

The Supporting Information is available free of charge on the ACS Publications website at DOI: 10.1021/acscatal.5b01045.

XRD, SECM, equivalent circuits, and capacitance and resistance plots (PDF)

■ AUTHOR INFORMATION

Corresponding Authors
*E-mail for V.D.S.: v.dalsanto@istm.cnr.it.
*E-mail for A.N.: a.naldoni@istm.cnr.it.

Notes
The authors declare no competing financial interest.

■ ACKNOWLEDGMENTS

■ REFERENCES

(1) Sivula, K. *J. Phys. Chem. Lett.* **2013**, *4*, 1624−1633.
(2) McKone, J. R.; Lewis, N. S.; Gray, H. B. *Chem. Mater.* **2014**, *26*, 407−414.
(3) Chen, S.; Wang, L.-W. *Chem. Mater.* **2012**, *24*, 3659−3666.
(4) Li, Z.; Luo, W.; Zhang, M.; Feng, J.; Zou, Z. *Energy Environ. Sci.* **2013**, *6*, 347−370.
(5) Sivula, K.; Le Formal, F.; Grätzel, M. *ChemSusChem* **2011**, *4*, 432−449.
(6) Barroso, M.; Mesa, C. A.; Pendlebury, S. R.; Cowan, A. J.; Hisatomi, T.; Sivula, K.; Grätzel, M.; Klug, D. R.; Durrant, J. R. *Proc. Natl. Acad. Sci. U. S. A.* **2012**, *109*, 15640−15640.
(7) Steier, L.; Herraiz-Cardona, I.; Gimenez, S.; Fabregat-Santiago, F.; Bisquert, J.; Tilley, S. D.; Grätzel, M. *Adv. Funct. Mater.* **2014**, *24*, 7681−7688.
(8) Le Formal, F.; Tétreault, N.; Cornuz, M.; Moehl, T.; Grätzel, M.; Sivula, K. *Chem. Sci.* **2011**, *2*, 737−743.
(9) Tilley, S. D.; Cornuz, M.; Sivula, K.; Grätzel, M. *Angew. Chem., Int. Ed.* **2010**, *49*, 6405−6408.
(10) Marelli, M.; Naldoni, A.; Minguzzi, A.; Allieta, M.; Virgili, T.; Scavia, G.; Recchia, S.; Psaro, R.; Dal Santo, V. *ACS Appl. Mater. Interfaces* **2014**, *6*, 11997−12004.
(11) Klahr, B.; Gimenez, S.; Fabregat-Santiago, F.; Bisquert, J.; Hamann, T. W. *J. Am. Chem. Soc.* **2012**, *134*, 16693−16700.
(12) Klahr, B.; Gimenez, S.; Fabregat-Santiago, F.; Bisquert, J.; Hamann, T. W. *Energy Environ. Sci.* **2012**, *5*, 7626−7636.
(13) Moniz, S. J. A.; Shevlin, S. A.; Martin, D. J.; Guo, Z.-X.; Tang, J. *Energy Environ. Sci.* **2015**, *8*, 731−759.
(14) Li, J.; Meng, F.; Suri, S.; Ding, W.; Huang, F.; Wu, N. *Chem. Commun.* **2012**, *48*, 8213−8215.
(15) Young, K. M. H.; Hamann, T. W. *Chem. Commun.* **2014**, *50*, 8727−8730.
(16) Gao, M.; Sheng, W.; Zhuang, Z.; Fang, Q.; Gu, S.; Jiang, J.; Yan, Y. *J. Am. Chem. Soc.* **2014**, *136*, 7077−7084.
(17) Smith, R. D. L.; Prévot, M. S.; Fagan, R. D.; Trudel, S.; Berlinguette, C. P. *J. Am. Chem. Soc.* **2013**, *135*, 11580−11586.
(18) Zhao, Z.; Wu, H.; He, H.; Xu, X.; Jin, Y. *Adv. Funct. Mater.* **2014**, *24*, 4698−4705.
(19) Louie, M. W.; Bell, A. T. *J. Am. Chem. Soc.* **2013**, *135*, 12329−12337.
(20) Trotochaud, L.; Ranney, J. K.; Williams, K. N.; Boettcher, S. W. *J. Am. Chem. Soc.* **2012**, *134*, 17253−17261.
(21) Lin, F.; Boettcher, S. W. *Nat. Mater.* **2013**, *13*, 81−86.
(22) Mills, T. J.; Lin, F.; Boettcher, S. W. *Phys. Rev. Lett.* **2014**, *112*, 148304.
(23) Kim, J. Y.; Magesh, G.; Youn, D. H.; Jang, J.-W.; Kubota, J.; Domen, K.; Lee, J. S. *Sci. Rep.* **2013**, *3*, 2681.
(24) Sivula, K.; Zboril, R.; Le Formal, F.; Robert, R.; Weidenkaff, A.; Tucek, J.; Frydrych, J.; Grätzel, M. *J. Am. Chem. Soc.* **2010**, *132*, 7436−7444.
(25) Kim, T. W.; Choi, K.-S. *Science* **2014**, *343*, 990−994.
(26) Minguzzi, A.; Alpuche-Aviles, M. A.; Rodríguez López, J.; Rondinini, S.; Bard, A. J. *Anal. Chem.* **2008**, *80*, 4055−4064.
(27) Smith, R. D. L.; Prévot, M. S.; Fagan, R. D.; Zhang, Z.; Sedach, P. A.; Siu, M. K. J.; Trudel, S.; Berlinguette, C. P. *Science* **2013**, *340*, 60−63.
(28) Li, Y.-F.; Selloni, A. *ACS Catal.* **2014**, *4*, 1148−1153.
(29) Doyle, R. L.; Godwin, I. J.; Brandon, M. P.; Lyons, M. E. G. *Phys. Chem. Chem. Phys.* **2013**, *15*, 13737−13783.
(30) Huang, J.-J.; Hwang, W.-S.; Weng, Y.-C.; Chou, T.-C. *Mater. Trans.* **2010**, *51*, 2294−2303.
(31) Corrigan, D. A. *J. Electrochem. Soc.* **1987**, *134*, 377−384.
(32) Corrigan, D. A.; Knight, S. L. *J. Electrochem. Soc.* **1989**, *136*, 613−619.
(33) Bard, A. J.; Mirkin, M. V. In *Scanning Electrochemical Microscopy*, 2nd ed.; CRC Press, Taylor & Francis Group: Boca Raton, FL, 2012; p 542.
(34) Maljusch, A.; Ventosa, E.; Rincón, R. A.; Bandarenka, A. S.; Schuhmann, W. *Electrochem. Commun.* **2014**, *38*, 142−145.
(35) Doyle, R. L.; Lyons, M. E.G. *Phys. Chem. Chem. Phys.* **2013**, *15*, 5224−5237.
(36) Losiewicz, B.; Budniok, A.; Rowinski, E.; Lagiewka, E.; Lasia, A. *Int. J. Hydrogen Energy* **2004**, *29*, 145−157.
(37) Upul Wijayantha, K. G.; Saremi-Yarahmadia, S.; Peter, L. M. *Phys. Chem. Chem. Phys.* **2011**, *13*, 5264−5270.
(38) Lopes, T.; Andrade, L.; Aguilar Ribeiro, H.; Mendes, A. *Int. J. Hydrogen Energy* **2010**, *35*, 11601−11608.
(39) Shimizu, K.; Lasia, A.; Boily, J.-F. *Langmuir* **2012**, *28*, 7914−7920.
(40) Ratcliff, E. L.; Meyer, J.; Steirer, K. X.; Garcia, A.; Berry, J. J.; Ginley, D. S.; Olson, D. C.; Kahn, A.; Armstrong, N. R. *Chem. Mater.* **2011**, *23*, 4988−5000.
(41) Kennedy, J.; Frese, K. *J. Electrochem. Soc.* **1978**, *125*, 723−726.
(42) Badia-Bou, L.; Mas-Marza, E.; Rodenas, P.; Barea, E. M.; Fabregat-Santiago, F.; Gimenez, S.; Peris, E.; Bisquert, J. *J. Phys. Chem. C* **2013**, *117*, 3826−3833.

(43) Klahr, B. M.; Hamann, T. W. *J. Phys. Chem. C* **2011**, *115*, 8393−8399.

(44) Dalle Carbonare, N.; Cristino, V.; Berardi, S.; Carli, S.; Argazzi, R.; Caramori, S.; Meda, L.; Tacca, A.; Bignozzi, C. A. *ChemPhysChem* **2014**, *15*, 1164−1174.